Biocompatible Nanoparticles Based on Diketo-Pyrrolo-Pyrrole (DPP) with Aggregation-Induced Red/NIR Emission for In Vivo Two-Photon Fluorescence Imaging

Yuting Gao, Guangxue Feng, Tao Jiang, Chiching Goh, Laiguan Ng, Bin Liu, Bo Li, Lin Yang, Jianli Hua,* and He Tian*

Compared with traditional one-photon fluorescence imaging, two-photon fluorescence imaging techniques have shown advantages such as increased penetration depth, lower tissue autofluorescence, and reduced photodamage, and therefore are particularly useful for imaging tissues and animals. In this work, the design and synthesis of two novel DPP-based compounds with large two-photon absorption (2PA) cross-sections ($\sigma \geq 8100$ GM) and aggregation-induced emission (AIE) properties are reported. The new compounds are red/NIR emissive and show large Stokes shifts ($\Delta\lambda \geq 3571$ cm^{-1}). 1,2-Distearoyl-*sn*-glycero-3-phosphoethanol amine-*N*-[maleimide(polyethylene glycol)-2000 (DSPE-PEG-Mal) is used as the encapsulation matrix to encapsulate DPP-2, followed by surface functionalization with cell penetrating peptide (CPP) to yield DPP-2-CPP nanoparticles with high brightness, good water dispersibility, and excellent biocompatibility. DPP-2 nanoparticles have been used for cell imaging and two-photon imaging with clear visualization of blood vasculature inside mouse ear skin with a depth up to 80 μm.

1. Introduction

Fluorescent probes have become invaluable tools in cell biology and medical imaging because of their high sensitivity and relatively inexpensiveness and easy maneuverability.[1] To fulfill the promise of increased temporal and spatial resolutions, considerable efforts have been made to improve fluorescence techniques. Fortunately, the emergence of two-photon fluorescence microscopy (2PFM)[2] has been one of the most prominent ameliorations in fluorescence imaging, which provides key advantages over conventional fluorescence imaging techniques, such as increased penetration depth, lower tissue autofluorescence, and reduced photodamage and photobleaching, making it particularly useful for imaging tissues and animals.[3] The fluorescence in the red/NIR region is also a prerequisite to avoid overlap with fluorescence of endogenous cell components and to improve the collection of the emitted light in thick samples.[4] Of particular significance are the fluorescent probes with both emission and excitation in the NIR (NIR-to-NIR) range, which have recently emerged as a new generation of nanoprobes for bioimaging.[5–7] These include organic dyes,[5] lanthanide complexes,[6] and many other nanoparticles[7] that suffer from either low two-photon brightness or limited molar absorptivity, posing a formidable hurdle to expand their biological applications.

Many materials synthesized with large 2PA cross-sections have coplanar structures and conformational rigidity.[8] Most of them are hydrophobic and their fluorescence quantum yields are considerably reduced in aggregated states, resulting from π–π stacking and other nonradiative pathways.[9] This phenomenon is known as aggregation-caused quenching (ACQ), which seriously limits their applications, especially in fluorescent chemosensors and bioimaging in vitro and in vivo.[10] Hence, a special molecular design for two-photon absorption (2PA) materials is required not only to ensure their large two-photon absorption cross sections (σ), but also to overcome fluorescence quenching at a high concentration or in an aggregated state. In 2001, Tang and co-workers[11] discovered a unique series of luminogens with aggregation-induced emission (AIE) characteristics. These AIE molecules behave exactly opposite to the conventional ACQ luminophores. They are nonemissive when molecularly dissolved in solvents but become highly luminescent when aggregated in the solid state. The development of these unique AIE luminogens sweeps away our concerns on emission quenching and promotes applications of organic

Y. Gao, T. Jiang, L. Yang, Prof. J. Hua, Prof. H. Tian
Key Laboratory for Advanced Materials
Institute of Fine Chemicals and Department of Chemistry
East China University of Science and Technology
130 Meilong Road, Shanghai 200237, P.R. China
E-mail: jlhua@ecust.edu.cn

G. Feng, Prof. B. Liu
Department of Chemical and Biomolecular Engineering
National University of Singapore
Singapore 117585, Singapore
E-mail: cheliub@nus.edu.sg

C. Goh, L. Ng
Singapore Immunology Network (SIgN)
A*STAR (Agency for Science, Technology and Research)
Biopolis, Singapore 138648, Singapore

Dr. B. Li
Key Laboratory of Polar Materials and Devices
Ministry of Education
East China Normal University
Shanghai 200241, P.R. China

DOI: 10.1002/adfm.201500010

compounds in fluorescent sensors and bioimaging.[12] Therefore, exploration of novel red/NIR fluorescent probes with optimized 2PA and AIE properties is highly desirable for in vivo imaging.

According to the proposed mechanism, most AIE luminogens are designed as propeller-shaped molecules because restriction of intramolecular rotations blocks the nonradiative pathway and opens up the radiative channel when aggregated. This is opposite to the general design strategy of 2PA materials, where planar structures with elongated conjugation generally favor large σ.[13] Therefore, it is difficult to find the right balance between optical properties and structures for optimized 2PA and AIE materials. Recently, a series of 2PA materials with AIE properties have been designed and synthesized.[14] However, these materials have small or moderate σ, and therefore strong laser power has to be used for imaging. To solve these problems, in this contribution, we designed and synthesized unique DPP-based red-emitting AIE materials with large σ. The large Stoke shifts, good biocompatibility, and high brightness make them promising fluorescent materials for in vitro and in vivo imaging. We further encapsulated the two dyes into organic nanoparticles via the modified nano-precipitation method, using (1,2-distearoyl-*sn*-glycero-3-phosphoethanolamine-*N*-[maleimide(polyethylene glycol)-2000]) (DSPE-PEG-Mal) as the encapsulation matrix,[15] and the organic nanoparticles could serve as an alternative to inorganic nanoparticles for two-photon fluorescence imaging.[16] Further surface functionalization with a cysteine-modified cell penetration peptide (CPP) with a peptide sequence of RKKKRRQRRRC yielded DPP-CPP nanoparticles with good water dispersibility and excellent biocompatibility.[17] The results indicate that the DSPE-PEG-Mal-encapsulated AIE nanoparticles can serve as efficient fluorescent probes for both one-photon and two-photon excited fluorescence imaging.

2. Results and Discussion

2.1. Molecular Design and Synthesis

DPP and its derivatives are widely used in the industry as high performance pigments, which show bright red fluorescence in a solution. Owing to their exceptional thermal and photochemical stability, large extinction coefficients, and high fluorescence quantum yields, DPP-based materials have received intensive research interests in the field of light-emitting diodes,[18] solar cells,[19] and biosensors.[20] However, it is a great challenge to sustain the efficient emission of DPP-based compounds in aggregated states due to the serious intermolecular π–π stacking. To overcome this problem, it is a rational strategy to attach bulky or AIE substituents onto DPP to hinder the ACQ effect.[21]

In our ongoing research on 2PA and AIE materials, we have recently shown a series of DPP-based 2PA materials possessing AIE characteristics with NIR emission; however, the σ values are generally lower than 500 GM.[22] To obtain effective 2PA materials, we introduced propeller-like starburst triphenylamine as a strong donor tethered to the central DPP acceptor via vinyl arm (**DPP-1**; **Scheme 1**). Compound **DPP-1** is AIE active and displays a high σ of 10 600 GM at 800 nm with an NIR emission maximum at 780 nm and a modest fluorescence quantum yield of 0.03 in solid state. We speculate that introducing an extended π-deficient phenylacrylonitrile could further block the good planarity to optimize the optical properties of the compound **DPP-2**. As expected, **DPP-2** shows a slightly decreased σ of 8100 GM at 800 nm, but a much higher quantum yield of 0.11 in a solid state, which makes it a promising 2PA probe for bioimaging.

The synthetic route to **DPP-1** and **DPP-2** is depicted in Scheme 1. Intermediate **1** was prepared according to the literature.[23a] To increase the solubility, the lactam groups were alkylated upon reaction with 1-bromobutane. Compound **2** was prepared by Suzuki coupling reaction between compound **1** and (4-(cyanomethyl)phenyl)boronic acid. The compound **DPP-1** was obtained by the Heck reaction between compound **2** and mutil-branched triphenylamine derivative **4**. **DPP-2** was prepared through a typical Knoevenagel condensation[24] between the triarylamine aldehyde **3** and compound **2**. Their structures were characterized by NMR and MS spectroscopies (Figures S8–S13, Supporting Information).

2.2. One-Photon Absorption and AIE Properties

Figure 1 shows the normalized one-photon absorption of 1×10^{-5} M **DPP-1** and **DPP-2** in THF as molecular species and

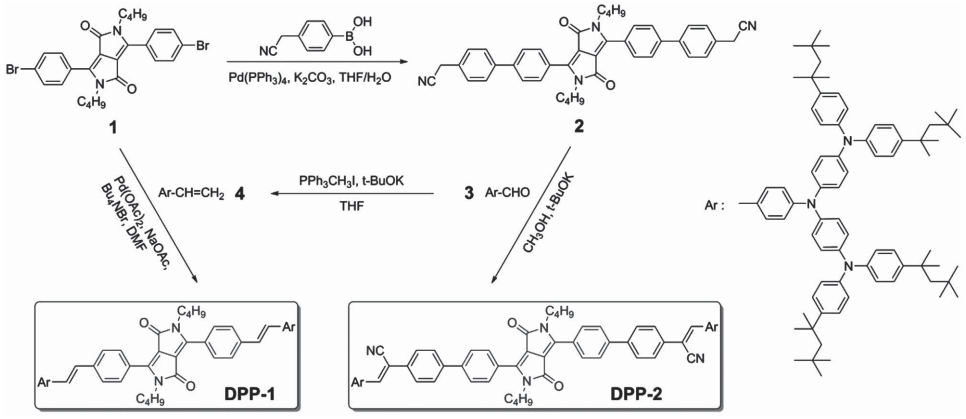

Scheme 1. Synthetic route to **DPP-1** and **DPP-2**.

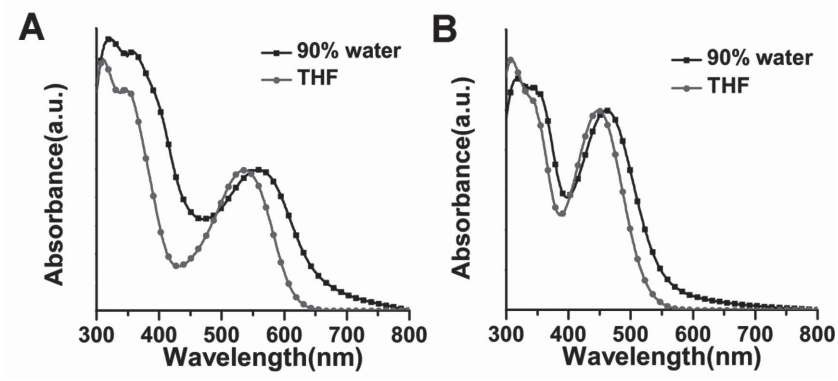

Figure 1. Normalized one-photon absorption of A) **DPP-1** and B) **DPP-2** in THF and in 90% water–THF mixture at 1×10^{-5} M.

in the THF/water mixture at 90% water content as aggregates. The absorption maxima (λ_{max}) of **DPP-1** and **DPP-2** in THF are located at 535 and 448 nm, and bathochromically shifted by 25 and 15 nm in an aggregated form (560 nm for **DPP-1** and 463 nm for **DPP-2**), respectively. The absorption tails extending well into the long wavelength region indicate that both **DPP-1** and **DPP-2** aggregate into particles in the presence of water, as it is well known that the Mie effect of nanoparticles can cause such level-off tails in the absorption spectra.[25] It is quite suprising that inserting the phenylacrylonitrile into the backbone results in an obvious hypochromic shift of 87 nm in THF. We suspect that in **DPP-2**, the phenylacrylonitrile instead of the DPP center acts as the acceptor. To test our hypothesis, a new dye of **ATCN** (Scheme S1, Supporting Information) with starburst triphenylamine as a donor and phenylacrylonitrile as an acceptor was synthsized. The absorption maximum of **ATCN** in THF is at 441 nm, which is similar to that of **DPP-2** (448 nm) (Figure S1, Supporting Information). These results reveal that in **DPP-2**, the phenylacrylonitriles indeed act as the main acceptors, favoring intramolecular charge transfer directly from triphenylamine to phenylacrylonitrile. In addition, the electrochemical behaviors of **DPP-1** and **DPP-2** were investigated by cyclic voltammetry using 0.1 M tetrabutylammonium hexafluorophosphate as a supporting electrolyte in the dichloromethane solution with platinum working electrodes, a platinum wire counter electrode, and a saturated calomel electrode (SCE) reference electrode. The SCE reference electrode was calibrated using a ferrocene/ferrocenium (Fc/Fc^+) redox couple as an external standard. It can be obtained from Figure S2 (Supporting Information) that the first half-wave potentials (E_{ox}) of **DPP-1** and **DPP-2** are 0.34 and 0.42 V, respectively. Therefore, the ground-state oxidation potentials corresponding to the HOMO energy levels are −5.04 and −5.12 (vs vacuum) according to the equations HOMO = −e (E_{ox} + 4.7) (eV), respectively. It is clear that the HOMO level of **DPP-2** is lower than that of **DPP-1**, which is due to the weaker electron-withdrawing ability of phenylacrylonitriles compared with the DPP unit (Table S1).

The absorption bands of **DPP-1** and **DPP-2** remain nearly identical in different solvents, such as hexane, toluene, dichloromethane (DCM), chloroform, and THF (Figure S3, Table S2, Supporting Information). With increased solvent polarity, the remarkable solvatochromism is concomitant with reduced fluorescence intensity (Figure S4, Table S3, Supporting Information), which is due to twisted intramolecular charge transfer (TICT) characteristics of both molecules.[26]

As expected, both **DPP-1** and **DPP-2** are AIE-active. **Figure 2**A shows the corresponding emission spectra of **DPP-1** in the THF-water mixture with different water fractions (f_w) at 1×10^{-5} M. The emission of **DPP-1** in the THF solution was very weak in that almost no photoluminescence (PL) signal was recorded. However, an increase in fluorescence was observed at f_w = 30%, and the PL signal was gradually enhanced upon increasing water-THF ratios. When f_w reached 90%, the PL intensity was boosted to the maximum with an NIR emission maximum at 700 nm. It was noted that the emission peak gradually blue-shifted from 780 to 700 nm when f_w

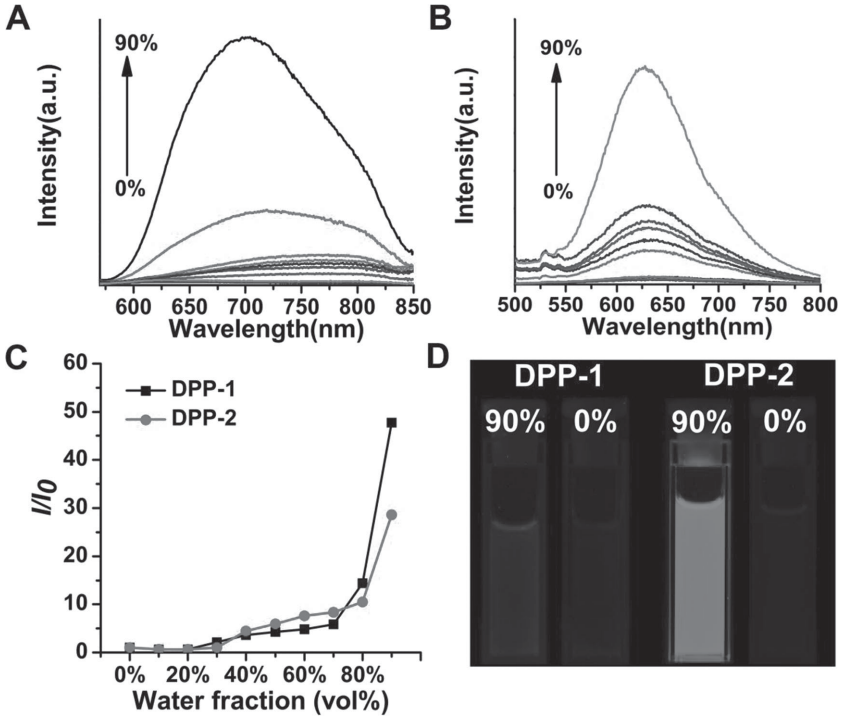

Figure 2. The emission spectra of A) **DPP-1** and B) **DPP-2** in THF–water mixtures with different water fractions at 1×10^{-5} M. Excitation wavelength: 550 nm for **DPP-1** and 455 nm for **DPP-2.** C) Plot of I/I_0 versus water content of the solvent mixture, where I_0 is the PL intensity in the pure THF solution. D) Photographs of **DPP-1** and **DPP-2** in the pure THF solution and the 90% water–THF mixture taken under illumination of a UV light.

was increased from 30 to 90%. Such a spectral shift can be explained as follows: with increased water content, **DPP-1** molecules started to aggregate, which generated less polar microenvironment for the molecules inside the aggregates. As **DPP-1** has a strong electron donor and an acceptor in the backbone, the reduced environment polarity led to the observed blue shift in the emission spectrum.[27] The similar behavior was also observed for **DPP-2** (Figure 2B) that a steep rise was shown when f_w reached up to 90% with a red emission maximum at 627 nm. At f_w = 90%, the PL intensities of **DPP-1** and **DPP-2** are 48-fold and 29-fold higher than their original emission intensities in THF, respectively (Figure 2C), indicating AIE characteristics for them, which is further evidenced by the solution fluorescence change (Figure 2D). In addition, the large Stokes shifts for **DPP-1** (3571 cm^{-1}) and **DPP-2** (5649 cm^{-1}) in aggregated states are favorable for bioimaging due to the minimized interference between excitation and emission.

For **DPP-1** and **DPP-2**, the formation of nanoparticles in THF/H_2O (1:9 v/v) was further verified by scanning electron microscopy (SEM) images (**Figure 3**A,B). The emission maxima of the **DPP-1** and **DPP-2** in solid state are at 780 and 660 nm with absolute quantum yields (Φ_f) of 0.03 and 0.11, respectively (Figure 3C,D). It should be noted that the introduction of phenylacrylonitrile leads to not only a larger Stokes shift but also a higher fluorescence. The photostabilities of **DPP-1** and **DPP-2** were studied using fluorescein isothiocyanate (FITC) as the control under continuous excitation with a 530 nm laser. The changes of the absorbance were monitored as a function of time with samples in quartz cuvettes (10 mm × 10 mm × 35 mm) (Figure S5, Supporting Information). The absorbance of **DPP-1** and **DPP-2** decreased much slower than that for FITC under light irradiation. The time-dependent variations in the absorbance ratio (A/A_0) of three dyes were also presented in Figure S5D (Supporting Information), which gives a clear picture of the time-dependent absorbance change for three dyes. After continuous light exposure for 60 min, the absorbance of the FITC solution dropped almost 30%, whereas the solutions of DPP-1 and DPP-2 showed only 3% and 8% decrease during the same period, respectively. The photodecomposition quantum yields, η, were subsequently calculated using the following equation:[28]

$$\eta = \frac{(A_1 - A_0)N_A}{\varepsilon I(1-10^{(A_1+A_0)/2})(t_1 - t_0)}$$

where η is the photochemical decomposition quantum yield, A_1 is the absorbance maximum at t_1, A_0 is the absorbance maximum at t_0, N_A is Avogadro's number, ε is molar absorbance in M^{-1} cm^{-1}, $(t_1 - t_0)$ is the time exposed (s), and I is the intensity of the laser in photon cm^{-2} s^{-1}.

From the results in **Table 1**, the photostability of the DPP dyes is nearly one order of magnitude higher than that for FITC. The good photostability of DPP-1 and DPP-2 makes them promising materials for bioimaging applications.

To further understand the optical properties of the compounds, the time-correlated single-photon counting method was used to elucidate the fluorescence decay of the **DPP**-based compounds in THF and the THF–water mixture solution

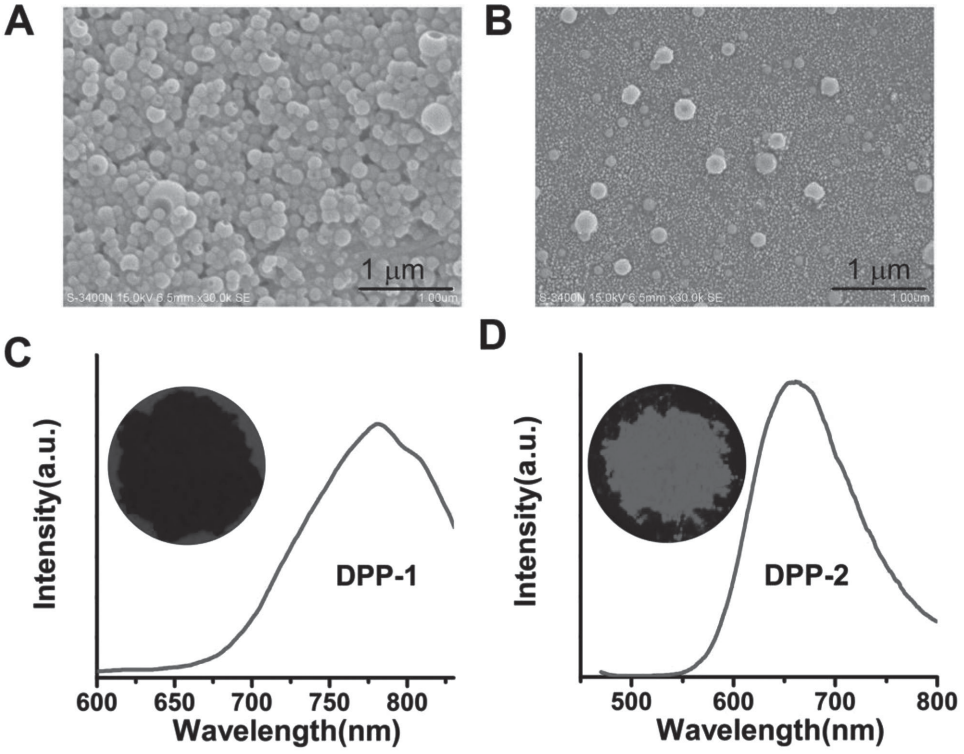

Figure 3. SEM images of A) DPP-1 and B) DPP-2 nanoaggregates prepared in THF/H_2O (1:9 v/v) at 1×10^{-5} M. Emission spectra of C) **DPP-1** and D) **DPP-2** as solid powders; excitation wavelength: 560 nm for **DPP-1** and 460 nm for **DPP-2.** Inset: photos of **DPP-1** and **DPP-2** powders taken under illumination of a UV light (excitation wavelength: 365 nm).

Table 1. Photochemical decomposition quantum yields (η) of **DPP-1**, **DPP-2**, and FITC.

Solvent	Dye	$\varepsilon^{a)}$ [M^{-1} cm^{-1}]	η
$CHCl_3$	**DPP-1**	5.49×10^4	5.23×10^{-5}
	DPP-2	6.41×10^4	6.38×10^{-5}
	FITC	1.27×10^4	4.81×10^{-4}

[a)][ε] Molar extinction coefficients.

(v/v = 1:9). As shown in Table S4, in the pure THF solution, the fluorescence decay of **DPP-1** is faster than the instrument response function of our system (≈100 ps), which indicates that intramolecular vibrational and torsional motions can act as efficient nonradiative pathways for the excited states to decay. In the 90% water–THF mixture solution, the fluorescence decay curve is well-fitted biexponentially with a decay time constant of ≈0.15 ns (0.10) and a rather long decay time constant of ≈1.36 ns (0.90). The phenomenon indicates that **DPP-1** molecules in the THF–water mixture solution decay through two relaxation pathways. The longer nanosecond decay components are attributed to the emission from the formed nanoaggregates that restrict the intramolecular motion.[29] The similar behavior was also observed for **DPP-2**. The trend of fluorescence lifetime changes from dye molecules to nanoparticles is similar to our previous report.[30]

2.3. Two-Photon Absorption Properties

The σ values of **DPP-1** and **DPP-2** were determined by the femtosecond open-aperture Z-scan technique according to the previous methods.[31] The repetition rate of the laser pulses is 1 kHz and the pulse duration is 80 fs. Figure S6 (Supporting Information) shows the open-aperture Z-scan data for **DPP-1** and **DPP-2**. The σ can be calculated by using the equation of $\sigma = h\nu\beta / N_0$, where $N_0 = N_A C$ is the number density of the absorption centers, N_A is the Avogadro constant, and C represents the solute molar concentration. Each dye was measured by three different pulse energies to give an average σ of 10 600 and 8100 GM at a wavelength of 800 nm for **DPP-1** and **DPP-2**, respectively. The introduced phenylacrylonitriles are able to block the good planarity of **DPP-2**, making the TICT process directly from triphenylamine to phenylacrylonitrile instead of to the DPP core, which results in slightly decreased σ compared with **DPP-1**. The two-photon fluorescence (2PF) spectra of **DPP-1** and **DPP-2** under different laser intensities are shown in Figure S7 (Supporting Information). The linear dependence of fluorescence intensity on the square of the excitation intensity, as shown in Figure S7C,D (Supporting Information), confirms that 2PA is the main excitation mechanism of the intense fluorescence emission.

Under the excitation of 80 fs, 800 nm pulse, **DPP-2** in a mixture of THF and water emits intense fluorescence with the maximum located at 650 nm (**Figure 4**A). The 2PF is slightly red-shifted as compared with one-photon excitation (627 nm) on account of reabsorption of partial emission. The one-photon excitation beam has a much shorter penetrating depth in the sample than that of the two-photon excitation laser beam, so

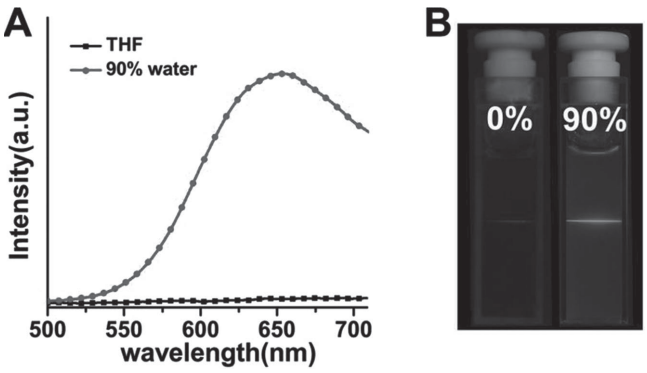

Figure 4. Two-photon fluorescence emission spectra (A) and 2PF images (B) for **DPP-2** in the solution (THF) and in dispersion of the nanoaggregate form (90% water) at 1×10^{-5} M excited at 800 nm.

that one-photon emission is from the sample surface and the reabsorption affects the fluorescence spectrum less as compared with that for 2PA.[32] As shown in Figure 4B, 2PF was remarkably intensified by the nanoaggregates formation.

2.4. Fabrication of DPP-Based NPs

Possessing the unique AIE feature, excellent 2PA capacity, large Stokes shift, good photostability, and high brightness in the red/NIR region, we chose **DPP-2** as the fluorescence probe for bioimaging. To endow it with good water solubility, **DPP-2** was encapsulated into polymer nanoparticles via a modified nanoprecipitation method using DSPE-PEG-Mal as the matrix. As illustrated in **Scheme 2**, to form the **DPP-2** nanoparticles, a THF mixture containing **DPP-2** and DSPE-PEG-Mal was diluted into MilliQ water under continuous ultrasound sonication. Upon mixing and dilution, the hydrophobic DSPE segment would intertwine with **DPP-2** to form the core, whereas the PEG chain would render outside toward water phase, rendering the nanoparticles with surface maleimide functional groups ready for further surface conjugation. After evaporation of THF, the nanoparticles were filtered through a 0.2 μm syringe filter, and concentrated under an argon flow upon continuous stirring. The obtained DPP-2 nanoparticles were well dispersed in the aqueous solution and stored at 4 °C.

The hydrodynamic diameters of **DPP-2** nanoparticles were studied by laser light scattering (LLS), suggesting an average size of ≈80 nm with a narrow size distribution (**Figure 5**A). High-resolution transmission electron microscopy (HR-TEM) was utilized to study their morphologies, which revealed uniform distributed spherical nanoparticles with mean diameters around 74 nm for **DPP-2** nanoparticles (Figure 5A, inset). It is worth noting that **DPP-2** nanoparticles are very stable in an aqueous solution as no large aggregation and obvious hydrodynamic diameter changes can be observed after they have been stored for several months. This should be ascribed to the existence of PEG chains outside particles that supress nonspecific interaction and further aggregation. The absorption and emission spectra of **DPP-2** nanoparticles are shown in Figure 5B, which exhibited similar spectra as when **DPP-2** was dispersed in the 90% water–THF mixture. It should be noted that the

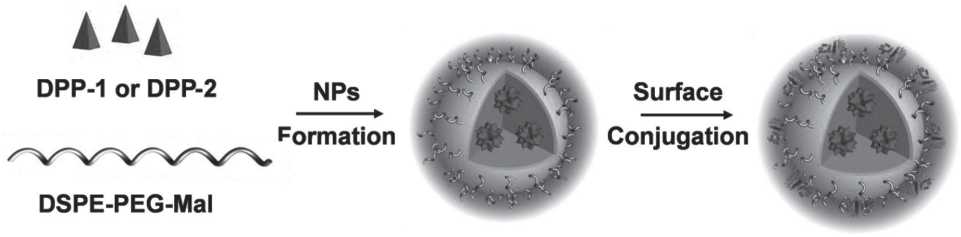

Scheme 2. Illustration of **DPP-1** or **DPP-2** nanoparticle formation, and surface functionalization with the cell penetration peptides (CCP) with the sequence of RKKRRQRRRC.

DPP-2 nanoparticles in water showed a Φ_f value of 0.12, measured using rhodamine B in ethanol as the standard, which is the same as that for their respective powders, indicating compact encapsulation of **DPP-2** in the nanoparticles. The 2PA spectra of these two NPs in water were also evaluated in the wavelength range of 800–960 nm. As shown in Figure 5C, the maxima of σ appear to be 5.34×10^5 GM for **DPP-2** NPs at 810 nm based on NP concentration, measured using Rhodamine 6G in methanol as the reference. In addition, the two-photon brightness per unit volume of **DPP-2** nanoparticles was also calculated to be 0.176 GM nm^{-3}.

2.5. One-Photon Cellular Imaging and Two-Photon Blood Vasculature Imaging

Inspired by the high two-photon fluorescence, large Stokes shift of **DPP-2** nanoparticles, we investigated their performance in one-photon cellular imaging and real-time two-photon blood vasculature imaging. The cellular imaging in vitro was studied by confocal laser scanning microscopy (CLSM). To enhance the cellular internalization ability, a cysteine-modified cell penetration peptide (CPP) with a peptide sequence of RKKRRQRRRC was conjugated to the **DPP-2** nanoparticle surface to yield **DPP-2-CPP** via the click reaction between the surface maleimide group and the thiol group on peptide. After incubation with **DPP-2-CPP** suspensions (0.5×10^{-9} M based on nanoparticle concentration) for 2 h at 37 °C in the culture medium, MCF-7 breast cancer cells were subsequently imaged by CLSM with 488 nm laser excitation and the fluorescent signals were collected above 505 nm. Strong red fluorescence from cell cytoplasm was observed (**Figure 6**A–D), suggesting efficient intracellular uptake of **DPP-2-CPP** nanoparticles. The 2PF image of **DPP-2-CPP**-treated MCF-7 cells was also obtained using 2PFM, where it showed very bright red fluorescence inside cellular cytoplasm (Figure S14, Supporting Information). It is of high importance that fluorescent probes have good biocompatibility with low cytotoxicity. The metabolic viability of MCF-7 cancer cells was further examined by methylthiazolyldiphenyltetrazolium bromide (MTT) assays, which revealed high cell viability of near 100% within 48 h even at a **DPP-2-CPP** nanoparticle concentration of 5×10^{-9} M, which is 10-fold higher than that used for imaging (Figure 6E).

2PFM was subsequently used to image blood vasculature of mouse ear. Before imaging, the **DPP-2** nanoparticles (24×10^{-9} M, 100 μL) were intravenously injected. **Figure 7**A shows the projection image and Figure 7B shows the 3D reconstructed image of the ear skin blood vessel image. As shown, upon two-photon excitation at 800 nm, bright red fluorescence from the whole blood vasculature network of mice ear dermis of the selected region is clearly observed. Moreover, not only the blood vessels, but also small capillaries, and even much deeply located arteries could be clearly observed by the **DPP-2** nanoparticles (Figure 7 C–F). It should be noted that the **DPP-2** nanoparticles at a size of ≈70 nm do not suffer from the leakage problem, which often happens to the widely used Evans blue, making the nanoparticles promising in the blood vessel-related imaging applications.

3. Conclusion

In summary, two novel **DPP**-based red/NIR AIE materials with large σ have been presented. By incorporating an extended

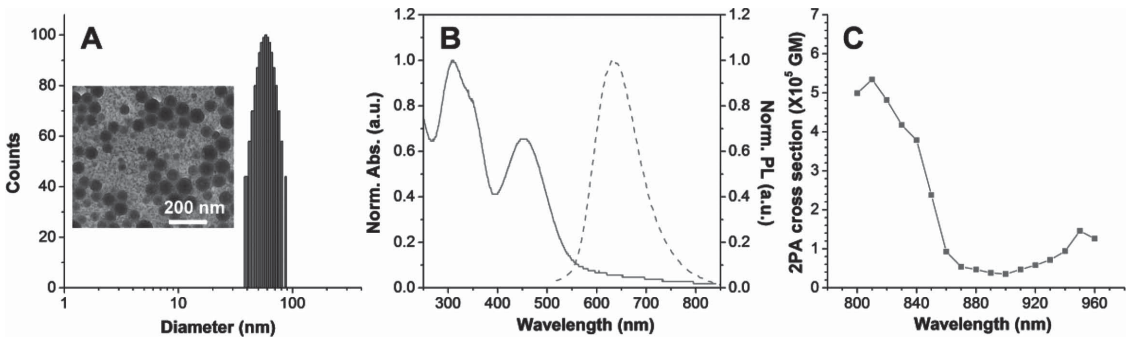

Figure 5. A) Laser light scattering and high-resolution TEM results. B) UV–vis and PL spectra. C) 2PA spectrum of **DPP-2**.

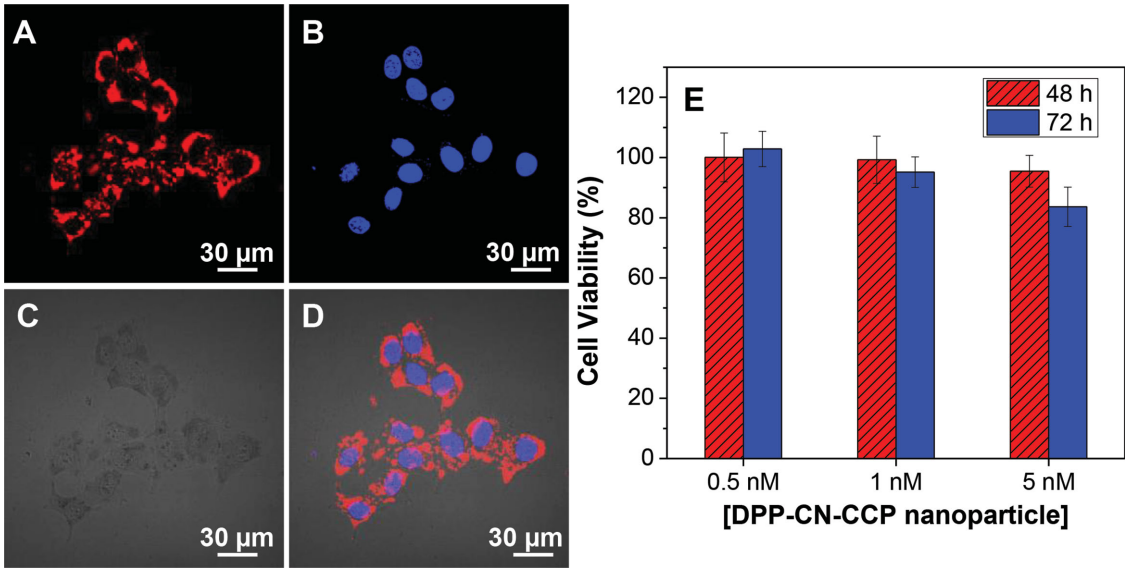

Figure 6. A–D) Confocal images of MCF-7 cells after incubation with 0.5×10^{-9} M **DPP-2-CPP** nanoparticles for 2 h at 37 °C. The nucleus was stained by Hoechst 33342 (blue, $\lambda_{ex} = 405$ nm, $\lambda_{em} = 430$–470 nm). E) Viability of MCF-7 cells after incubation with **DPP-2-CPP** nanoparticles (0.5, 1.0, 5.0×10^{-9} M, respectively) for 48 and 72 h at different concentrations.

π-deficient phenylacrylonitrile, **DPP-2** shows much shorter absorption/emission wavelengths, higher brightness, and larger Stokes shift as compared with those of **DPP-1**. **DPP-2** molecules with large σ, great AIE property, and high brightness, are encapsulated by DSPE-PEG-Mal into nanoparticles to render them with good water dispersibility and excellent biocompatibility. The **DPP-2** nanoparticles have been successfully used for cell imaging and two-photon blood vasculature imaging. The molecular design provides an effective strategy to efficient 2PA and AIE materials.

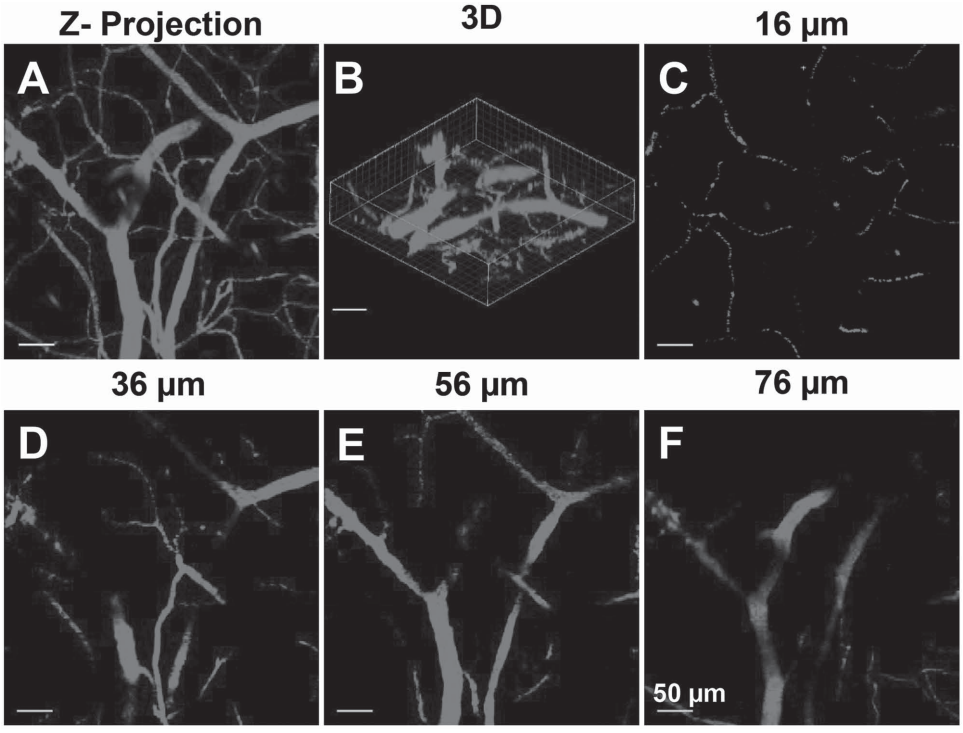

Figure 7. Two-photon fluorescence images of **DPP-2** nanoparticles stained blood vessels. A) Z-projection image of blood vessels in ear skin. B) 3D reconstructed blood vessels image. C–F) Image at different vertical depths of the ear skin. The fluorescence signal is collected using a filter set of 620/40 nm, upon excitation at 800 nm.

4. Experimental Section

Materials and Methods: Tetrahydrofuran (THF) was predried over 4 Å molecular sieves and distilled under argon atmosphere from sodium benzophenone ketyl immediately before use. Triethylamine was distillated under normal pressure and dried over potassium hydroxide. *N,N*-dimethyl formamide (DMF), dichloromethane (DCM), and chloroform were reflux with calcium hydride and distilled before being used. The important intermediates **1** and 4-[*N,N*-di(4-iodophenyl)amino]-benzaldehyde were obtained as reported earlier[22] and synthetic routes to **3** and **ATCN** were shown in Scheme S1 (Supporting Information). All other chemicals were purchased from Aldrich and used as received without further purification.

Instruments: ^{1}H and ^{13}C NMR spectra were recorded on a Bruker AM-500/AM-400 spectrometer using chloroform-*d* as a solvent and tetramethylsilane (δ = 0) as internal references. The UV–vis spectra were recorded on a Varian-Cary 500 spectrophotometer with 2 nm resolution at room temperature and a Shimadzu UV-1700 spectrometer. The fluorescence spectra were taken on a Varian–Cary fluorescence spectrophotometer and a Perkin-Elmer LS 55 spectrofluorometer. The SEM micrographs were obtained on a JEOL JSM-6360 scanning electron microscope (SEM). Average particle size and size distribution of the samples were measured by laser light scattering (LLS) with a particle size analyzer (90 Plus, Brookhaven Instruments Co., USA) at a fixed angle of 90° at room temperature. The morphology of the samples was studied by transmission electron microscopy (TEM, JEM-2010F, JEOL, Japan).

Synthesis of 2,2′-((2,5-Dibutyl-3,6-dioxo-2,3,5,6-tetrahydropyrrolo[3,4-c]-pyrrole-1,4-diyl)bis([1,1′-biphenyl]-4′,4-diyl))diacetonitrile ***(2)***: In a 100 mL two-necked round-bottom flask, compound **1** (446 mg, 0.8 mmol) was dissolved in 30 mL of THF and followed with 1 mL of the 2 M potassium carbonate aqueous solution under argon atmosphere. After stirring for 1 h at 60 °C, (4-(cyanomethyl)phenyl)boronic acid (122 mg, 1 mmol) was dissolved in 10 mL of THF and added to the mixture dropwise. After stirring for another 15 h at 80 °C, the mixture was extracted with water and DCM. The combined organic phases were dried over anhydrous $MgSO_4$ and concentrated using a rotary evaporator. The residue was purified by column chromatography on silica (petroleum ether:dichloromethane = 1:4, v/v) to afford 300 mg of product as an orange-red powder (yield: 56%). ^{1}H NMR ($CDCl_3$, 400 MHz), δ(TMS, ppm): 7.94 (d, J = 8.4 Hz, 4H), 7.76 (d, J = 8.4 Hz, 4H), 7.67 (d, J = 8.2 Hz, 4H), 7.46 (d, J = 8.2 Hz, 4H), 3.98–3.67 (m, 8H), 1.78–1.58 (m, 4H), 1.44–1.18 (m, 4H), 0.88 (t, J = 7.4 Hz, 6H). ^{13}C NMR ($CDCl_3$, 101 MHz), δ (TMS, ppm): 162.82, 148.02, 142.80, 139.89, 129.85, 129.34, 128.71, 128.02, 127.37, 117.73, 110.12, 42.00, 31.70, 23.62, 20.06, 13.57. HRMS (ESI) (m/z): $[M+H]^+$ calculated for $C_{42}H_{38}N_4O_2$, 631.2995; found: 631.3071.

Synthesis of N1-(4-(bis(4-(2,4,4-Trimethylpentan-2-yl)phenyl)amino)-phenyl)-N4,N4-bis(4-(2,4,4-trimethylpentan-2-yl)phenyl)-N1-(4-vinylphenyl)-benzene-1,4-diamine ***(4)***: In a 100 mL two-necked round-bottom flask, 808 mg (5.6 mmol) of methyltriphenylphosphonium iodide, 224 mg (2 mmol) of sodium methanolate were dissolved in 20 mL of dry THF followed under argon atmosphere. After stirring for 10 min at 0 °C, compound **3** (1055 mg, 1 mmol) was dissolved in 10 mL of THF and added to the mixture dropwise. After stirring for another 2 h at room temperature, hydrochloric acid was added to adjust PH of the mixture to 7. Then, the mixture was extracted with water and DCM. The combined organic phases were dried over anhydrous $MgSO_4$ and concentrated using a rotary evaporator. The residue was purified by column chromatography on silica (petroleum ether:dichloromethane = 5:1, v/v) to afford 650 mg of product as a white powder (yield: 61%). ^{1}H NMR (THF-d_8, 400 MHz), δ (TMS, ppm): 7.15 (d, J = 8.3 Hz, 10H), 6.96–6.67 (m, 18H), 6.52 (dd, J = 17.5, 10.9 Hz, 1H), 5.49 (d, J = 17.6 Hz, 1H), 4.95 (d, J = 10.9 Hz, 1H), 1.63 (s, 8H), 1.25 (s, 24H), 0.65 (s, 36H). ^{13}C NMR (THF-d_8, 126 MHz), δ (TMS, ppm): 147.83, 145.23, 143.82, 143.46, 141.96, 136.42, 131.13, 126.82, 126.79, 125.16, 124.24, 123.14, 122.06, 110.52, 56.86, 37.88, 32.07, 31.21, 31.00. HRMS (ESI) (m/z): $[M]^+$ calculated for $C_{76}H_{99}N_3$, 1053.7839; found: 1053.7838.

Synthesis of 3,6-bis(4-(bis(4-(bis(4-Octylphenyl)amino)phenyl)amino)-styryl)phenyl)-2,5-dibutylpyrrolo[3,4-c]pyrrole-1,4(2H,5H)-dione ***(DPP-1)***: In a two-necked round-bottom flask, compound **2** (60 mg, 0.1 mmol), compound **5** (265 mg, 0.25 mmol), $Pd(OAc)_2$ (16 mg), NaOAc (1.62 g), and n-Bu_4NBr (126 mg) were dissolved in 30 mL of DMF under argon atmosphere. The mixture was heated to 100 °C for 48 h. After that, the mixture was poured into water to get a precipitate. The crude product was purified by column chromatography on silica (petroleum ether:dichloromethane = 1:2, v/v) to afford 115 mg of product as a red powder (yield: 53.4%). ^{1}H NMR (THF-d_8, 400 MHz), δ (TMS, ppm): 7.84 (d, J = 8.1 Hz, 4H), 7.56 (d, J = 8.5 Hz, 4H), 7.34 (d, J = 8.5 Hz, 4H), 7.16 (d, J = 8.5 Hz, 16H), 7.00 (d, J = 16.3 Hz, 4H), 6.96–6.77 (m, 36H), 3.76 (t, J = 5.9 Hz, 4H), 1.64 (s, 16H), 1.52–1.38 (m, 4H), 1.25 (s, 48H), 1.17–1.02 (m, 4H), 0.65 (s, 78H). ^{13}C NMR (THF-d_8, 101 MHz), δ (TMS, ppm): 161.97, 146.83, 145.20, 143.95, 140.62, 129.11, 127.60, 126.85, 126.13, 125.54, 124.13, 123.27, 109.82, 56.86, 37.90, 32.09, 31.48, 31.22, 31.02, 29.63, 19.82, 13.06. MALDI-TOF (m/z): $[M]^+$ calculated for $C_{178}H_{222}N_8O_2$, 2504.7549; found: 2504.7982.

Synthesis of 2,2′-((2,5-Dibutyl-3,6-dioxo-2,3,5,6-tetrahydropyrrolo[3,4-c]pyrrole-1,4-diyl)bis([1,1′-biphenyl]-4′,4-diyl))bis(3-(4-(bis(4-(bis(4-octylphenyl)amino)phenyl)amino)phenyl)acrylonitrile) ***(DPP-2)***: A mixture of compound 3 (120 mg, 0.2 mmol), compound 4 (534 mg, 0.48 mmol), and potassium tert-butoxide (112 mg, 1.0 mmol) was dissolved in 30 mL of methanol. This mixture was stirred for 24 h at a reflux temperature under an atmosphere of argon. Upon cooling, an orange solid precipitate was filtered, washed with cold methanol, and purified by column chromatography on silica (DCM/petroleum ether = 1/1, v/v) to yield 140 mg of product as an orange solid (yield: 26%). ^{1}H NMR (THF-d_8, 400 MHz), δ (TMS, ppm): 7.76 (d, J = 7.4 Hz, 4H), 7.72–7.63 (m, 10H), 7.60 (d, J = 6.3 Hz, 4H), 7.37 (d, J = 8.2 Hz, 2H), 7.31 (d, J = 8.3 Hz, 2H), 7.19 (d, J = 8.6 Hz, 16H), 7.02–6.80 (m, 36H), 3.56 (t, J = 8.0 Hz, 4H), 1.65 (s, 16H), 1.49–1.41 (m, 4H), 1.26 (s, 48H), 1.13–1.01 (m, 4H), 0.66 (s, 78H). ^{13}C NMR (THF-d_8, 101 MHz), δ (TMS, ppm): 161.10, 150.42, 145.04, 144.33, 140.24, 140.12, 130.71, 130.64, 129.30, 127.18, 127.03, 126.93, 126.75, 125.87, 125.73, 123.65, 118.72, 105.97, 98.45, 56.85, 37.97, 32.70, 32.08, 31.21, 31.98, 29.67, 19.67, 13.08. MALDI-TOF (m/z): $[M+2Na]^{2+}$ calculated for $C_{192}H_{228}N_{10}O_2$, 2753.9101; found, 2753.9363.

Synthesis of DPP-1 and DPP-2 Nanoparticles: The **DPP-1** nanoparticles were prepared via a modified nanoprecipitation method. 1 mL of the THF solution containing DSPE-PEG-Mal (2 mg) and **DPP-1** (1 mg) dropwise was added to 10 mL of MilliQ water, under ultrasound sonication at 12 W output using a microtip probe sonicator (XL2000, Misonix Incorporated, NY). The mixture was then stirred at 600 rpm at room temperature in dark overnight for the evaporation of THF. The formed NP suspension was then filtered through a 200 nm syringe filter. The **DPP-1** nanoparticles were further concentrated under Argon flow stirring at 600 rpm. Same procedures were repeated for **DPP-2** nanoparticles.

Synthesis of DPP-2-CCP Nanoparticles: 4 mL of the **DDP-2** nanoparticle solution was reacted with 6.40 µL of CPP (0.02 M, DMSO). After overnight reaction under stirring at room temperature, the solution was dialyzed against MilliQ water by 6000–8000 kDa membrane for 3 d to remove excess CPP and DMSO.

Cell Culture: MCF-7 breast cancer cells were cultured in DMEM containing 10% fetal bovine serum and 1% penicillin streptomycin at 37 °C in a humidified environment containing 5% CO_2. Before experiments, the cells were precultured until confluence was reached.

Cellular Imaging: MCF-7 breast cancer cells were cultured in an 8-well confocal plate at 37 °C. After 80% confluence, the medium was removed, and the adherent cells were washed twice with the 1× PBS buffer. **DPP-2-CPP** (0.5×10^{-9} M based on NP concentration) in the cell culture medium was then added to the wells. After 2 h incubation at 37 °C, the cells were washed twice with the 1× PBS buffer. Hoechst 33342 (Invitrogen, 2 µg mL^{-1}) was added to the wells. After 30 min incubation, the cells were further washed twice with the 1× PBS buffer and imaged by CLSM (Zeiss LSM 410, Jena, Germany) with imaging software (Fluoview FV1000). The signal of Hoechst 33342 was collected

between 430 and 470 nm upon excitation at 405 nm. The signal of **DPP-2-CPP** was collected above 505 nm upon excitation at 488 nm.

*Cytotoxicity of **DPP-2-CPP***: The metabolic activity of MCF-7 breast cancer cells was evaluated using methylthiazolyldiphenyltetrazolium bromide (MTT) assays. MCF-7 cancer cells were seeded in 96-well plates (Costar, IL) at an intensity of 4×10^4 cells mL^{-1}, respectively. After 24 h incubation, the old medium was replaced by **DPP-2-CPP** suspension at concentrations of 0.5, 1.0, 5.0×10^{-9} M, and the cells were then incubated for 48 and 72 h, respectively. Then, the wells were washed with the 1× PBS buffer and 100 µL of freshly prepared MTT (0.5 mg mL^{-1}) solution in the culture medium was added to each well. The MTT medium solution was carefully removed after 3 h incubation in the incubator. Filtered DMSO (100 µL) was then added to each well, and the plate was gently shaken for 10 min at room temperature to dissolve all the precipitates formed. The absorbance of MTT at 570 nm was monitored by the microplate reader (Genios Tecan). Cell viability was expressed by the ratio of the absorbance of the cells incubated with **DPP-2-CPP** NPs to that of the cells incubated with the culture medium only.

Blood Vasculature Imaging: Hair is thoroughly removed using hair removal cream before placing the ear on a heating platform that maintains the physiological temperature of the ear at 35 °C. For two-photon fluorescence imaging (2PFI) experiments, mice were anesthetized (150 mg kg^{-1} ketamine and 10 mg kg^{-1} xylazine) and placed on a heating pad to maintain a core body temperature of 37 °C throughout each imaging procedure. 100 µL of **DPP-2** nanoparticles at a concentration of 24×10^{-9} M based on NP concentration was administered via retro-orbital injection before imaging. All procedures were performed under the institution's Institutional Animal Care and Use Committee (IACUC) guidelines. A TriM Scope II single-beam two-photon microscope (LaVision BioTec) with a tuneable 680–1080 nm laser (Coherent) was used to acquire the images.

Supporting Information

Supporting Information is available from the Wiley Online Library or from the author.

Acknowledgements

Y.G. and G.F. contributed equally to this work. This work was supported by the National Basic Research 973 Program (2013CB733700 and 2013CB834701), NSFC/China (21421004, 21372082, 21172073, and 91233207), the Singapore JCO (IMRE/14-8P1110), SMART (R279-000-378-592), and the Singapore Ministry of Defense (R279-000-340-232).

Received: January 1, 2015
Published online: March 30, 2015

[1] R. W. Sinkeldam, N. J. Greco, Y. Tor, *Chem. Rev.* **2010**, *110*, 2579.
[2] W. Denk, J. Strickler, W. Webb, *Science* **1990**, *248*, 73.
[3] a) F. Helmchen, W. Denk, *Nat. Methods* **2005**, *2*, 932; b) D. R. Larson, W. R. Zipfel, R. M. Williams, S. W. Clark, M. P. Bruchez, F. W. Wise, W. W. Webb, *Science* **2003**, *300*, 1434; c) M. Komatsu, K. D. Belfield, *Biomaterials* **2012**, *33*, 8477; d) H. Yan, L. He, C. Ma, J. Li, J. Yang, R. Yang, W. Tan, *Chem. Commun.* **2014**, *50*, 8398; e) S. Li, X. Shen, L. Li, P. Yuan, Z. Guan, S. Q. Yao, Q.-H. Xu, *Langmuir* **2014**, *30*, 7623.
[4] a) D. Ding, K. Li, W. Qin, R. Zhan, Y. Hu, J. Liu, B. Z. Tang, B. Liu, *Adv. Healthcare Mater.* **2013**, *2*, 500; b) S. Kim, Y. T. Lim, E. G. Soltesz, A. M. D. Grand, J. Lee, A. Nakayama, J. A. Parker, T. Mihaljevic, R. G. Laurence, D. M. Dor, L. H. Cohn, M. G. Bawendi, J. V. Frangioni, *Nat. Biotechnol.* **2004**, *22*, 93; c) X. H. Gao, Y. Y. Cui, R. M. Levenson, L. W. K. Chung, S. M. Nie, *Nat. Biotechnol.* **2004**, *22*, 969.
[5] a) M.-Q. Zhu, G.-F. Zhang, C. Li, M. P. Aldred, E. Chang, R. A. Drezek, A. D. Q. Li, *J. Am. Chem. Soc.* **2011**, *133*, 365; b) J. Massin, A. Charaf-Eddin, F. Appaix, Y. Bretonniere, D. Jacquemin, B. Sanden, C. Monnereau, C. Andrauda, *Chem. Sci.* **2013**, *4*, 2833; c) A. D'Aléo, A. Felouat, V. Heresanu, A. Ranguis, D. Chaudanson, A. Karapetyan, M. Giorgic, F. Fages, *J. Mater. Chem. C* **2014**, *2*, 5208.
[6] a) T. Zhang, X. Zhu, C. C. W. Cheng, W.-M. Kwok, H.-L. Tam, J. Hao, D. W. J. Kwong, W.-K. Wong, K.-L. Wong, *J. Am. Chem. Soc.* **2011**, *133*, 20120; b) A. D'Aléo, A. Bourdolle, S. Brustlein, T. Fauquier, A. Grichine, A. Duperray, P. L. Baldeck, C. Andraud, S. Brasselet, O. Maury, *Angew. Chem. Int. Ed.* **2012**, *51*, 6622; c) G. Lapadula, A. Bourdolle, F. Allouche, M. P. Conley, I. Rosal, L. Maron, W. W. Lukens, Y. Guyot, C. Andraud, S. Brasselet, C. Copéret, O. Maury, R. A. Andersen, *Chem. Mater.* **2014**, *26*, 1062.
[7] a) J. Qian, D. Wang, F. Cai, Q. Zhan, Y. Wang, S. He. *Biomaterials* **2012**, *33*, 4851; b) X. Wang, A. R. Morales, T. Urakami, L. Zhang, M. V. Bondar, M. Komatsu, K. D. Belfield, *Bioconjugate Chem.* **2011**, *22*, 1438.
[8] a) M. Pawlicki, H. A. Collins, R. G. Denning, H. L. Anderson, *Angew. Chem. Int. Ed.* **2009**, *48*, 3244; b) G. S. He, L.-S. Tan, Q. Zheng, P. N. Prasad, *Chem. Rev.* **2008**, *108*, 1245; c) S. Sumalekshmy, J. F. Christoph, *Chem. Mater.* **2011**, *23*, 483.
[9] a) S. A. Jenekhe, J. A. Osaheni, *Science* **1994**, *265*, 765; b) C. Wu, H. Peng, Y. Jiang, J. McNeill, *J. Phys. Chem. B* **2006**, *110*, 14148.
[10] a) C. L. Chiang, S.-M. Tseng, C. T. Chen, C. P. Hsu, C. F. Shu, *Adv. Funct. Mater.* **2008**, *18*, 248; b) B. S. Gaylord, S. Wang, A. J. Heeger, G. C. Bazan, *J. Am. Chem. Soc.* **2001**, *123*, 6417.
[11] J. Luo, Z. Xie, J. W. Y. Lam, L. Cheng, H. Chen, C. Qiu, H. S. Kwok, X. Zhan, Y. Liu, D. Zhu, B. Z. Tang, *Chem. Commun.* **2001**, *21*, 1740.
[12] a) X. G. Gu, G. X. Zhang, D. Q. Zhang, *Analyst* **2012**, *137*, 365; b) Y. H. Li, Y. Q. Wu, J. Chang, M. Chen, R. Liu, F. Y. Li, *Chem. Commun.* **2013**, *49*, 11335; c) S. Chen, Y. Hong, Y. Liu, J. Liu, C. W. T. Leung, M. Li, R. T. K. Kwok, E. Zhao, J. W. Y. Lam, Y. Yu, B. Z. Tang, *J. Am. Chem. Soc.* **2013**, *135*, 4926; d) D. Ding, K. Li, B. Liu, B. Z. Tang, *Acc. Chem. Res.* **2013**, *46*, 2441; e) Y. Yuan, T. K. K. Ryan, B. Z. Tang, B. Liu, *J. Am. Chem. Soc.* **2014**, *136*, 2546; f) K. Li, B. Liu, *Chem. Soc. Rev.* **2014**, *43*, 6570; g) H. Shi, R. Kwok, J. Liu, B. Xing, B. Z. Tang, B. Liu, *J. Am. Chem. Soc.* **2012**, *134*, 17972; h) H. Shi, J. Liu, J. Geng, B. Z. Tang, B. Liu, *J. Am. Chem. Soc.* **2012**, *134*, 9569.
[13] a) M. Maurin, L. Vurth, J. Vial, P. Baldeck, S. R. Marder, B. V. Sanden, O. Stephan, *Nanotechnology* **2009**, *20*, 235102; b) Y. Hong, J. W. Y. Lam, B. Z. Tang, *Chem. Commun.* **2009**, *29*, 4332; c) K. Li, Y. Jiang, D. Ding, X. Zhang, Y. Liu, J. Hua, S.-S. Feng, B. Liu, *Chem. Commun.* **2011**, *47*, 7323.
[14] a) B. Xu, M. Xie, J. He, B. Xu, Z. Chi, J. W. Tian, L. Jiang, F. Zhao, S. Liu, Y. Zhang, Z. Xu, J. Xu, *Chem. Commun.* **2013**, *49*, 273; b) J. Geng, K. Li, D. Ding, X. Zhang, W. Qin, J. Liu, B. Z. Tang, B. Liu, *Small* **2012**, *8*, 3655; c) Y. Wang, T. Liu, L. Bu, J. Li, C. Yang, X. Li, Y. Tao, W. Yang, *J. Phys. Chem. C* **2012**, *116*, 15576; d) D. Ding, C. C. Goh, G. Feng, Z. Zhao, J. Liu, R. Liu, N. Tomczak, J. Geng, B. Z. Tang, L. G. Ng, B. Liu, *Adv. Mater.* **2013**, *25*, 6083; e) K. Li, W. Qin, D. Ding, N. Tomczak, J. Geng, R. Liu, J. Liu, X. Zhang, H. Liu, B. Liu, B. Z. Tang, *Sci. Rep.* **2013**, *3*, 1150.
[15] a) G. Feng, K. Li, J. Liu, D. Ding, B. Liu, *Small* **2014**, *10*, 1212; b) G. Feng, C. Y. Tay, Q. X. Chui, R. Liu, N. Tomczak, J. Liu, B. Z. Tang, D. T. Leong, B. Liu, *Biomaterials* **2014**, *35*, 8669.
[16] M. Geszke-Moritz, H. Piotrowska, M. Murias, L. Balan, M. Moritz, J. Lulek, R. Schneider, *J. Mater. Chem. B* **2013**, *1*, 698.
[17] a) K. Li, Z. Zhu, P. Cai, R. Liu, N. Tomczak, D. Ding, J. Liu, W. Qin, Z. Zhao, Y. Hu, X. Chen, B. Z. Tang, B. Liu, *Chem. Mater.* **2013**, *25*,

4181; b) S. Piantavigna, G. A. McCubbin, S. Boehnke, B. Graham, L. Spiccia, L. L. Martin, *Biochim. Biophys. Acta.* **2011**, *1808*, 1811.
[18] J. S. Ha, K. H. Kim, D. H. Choi, *J. Am. Chem. Soc.* **2011**, *133*, 10364
[19] N. Y. Kwon, G. Jang, J. Kim, D. Kim, T. S. Lee, *J. Polym. Sci., Part A: Polym. Chem.* **2013**, *51*, 2393.
[20] Y. Qu, Y. Q. Wu, Y. T. Gao, S. Y. Qu, L. Yang, J. L. Hua, *Sens. Actuators B-Chem.* **2014**, *197*, 13.
[21] a) X. Q. Li, X. Zhang, S. Ghosh, F. Würthner, *Chem. Eur. J.* **2008**, *14*, 8074; b) Y. Che, X. Yang, K. Balakrishnan, J. Zuo, L. Zang, *Chem. Mater.* **2009**, *21*, 2930; c) Q. Zhao, K. Li, S. Chen, A. Qin, D. Ding, S. Zhang, Y. Liu, B. Liu, J. Z. Sun, B. Z. Tang, *J. Mater. Chem.* **2012**, *22*, 15128.
[22] B. Wang, N. N. He, B. Li, S. Y. Jiang, Y. Qu, S. Y. Qu, H. Tian, J. L. Hua, *Aust. J. Chem.* **2012**, *65*, 387.
[23] a) S. Y. Qu, W. J. Wu, J. L. Hua, H. Tian, *J. Phys. Chem. C* **2010**, *114*, 1343; b) Y. H. Jiang, Y. C. Wang, J. L. Hua, J. Tang, B. Li, S. X. Qian, H. Tian, *Chem. Commun.* **2010**, *46*, 4689.
[24] a) G. A. Sotzing, C. A. Thomas, J. R. Reynolds, P. J. Steel, *Macromolecules* **1998**, *31*, 3750; b) S. C. Moratti, R. Cervini, A. B. Holmes, D. R. Baigent, R. H. Friend, N. C. Greenham, J. Gruner, P. J. Hamer, *Synth. Met.* **1995**, *71*, 2117.
[25] B. Z. Tang, Y. Geng, J. W. Y. Lam, B. Li, X. Jing, X. Wang, F. Wang, A. B. Pakhomov, X. Zhang, *Chem. Mater.* **1999**, *11*, 1581.
[26] a) Z. R. Grabowski, K. Rotkiewicz, W. Rettig, *Chem. Rev.* **2003**, *103*, 3899; b) X. Y. Shen, W. Z. Yuan, Y. Liu, Q. Zhao, P. Lu, Y. Ma, I. D. Williams, A. Qin, J. Z. Sun, B. Z. Tang, *J. Phys. Chem. C* **2012**, *116*, 10541; c) W. Qin, D. Ding, J. Liu, W. Z. Yuan, Y. Hu, B. Liu, B. Z. Tang, *Adv. Funct. Mater.* **2012**, *22*, 771.
[27] a) X. Y. Shen, Y. Wang, E. Zhao, W. Yuan, Y. Liu, P. Lu, A. Qin, Y. Ma, J. Sun, B. Z. Tang, *J. Phys. Chem. C* **2013**, *117*, 7334; b) W. Z. Yuan, Y. Gong, S. Chen, X. Y. Shen, J. W. Y. Lam, P. Lu, Y. Lu, Z. Wang, R. Hu, Ni Xie, H. S. Kwok, Y. Zhang, J. Z. Sun, B. Z. Tang, *Chem. Mater.* **2012**, *24*, 1518.
[28] a) H.-Y. Ahn, S. Yao, X. Wang, K. D. Belfield, *ACS Appl. Mater. Interfaces* **2012**, *4*, 2847; b) C. C. Corredor, K. D. Belfield, M. V. Bondar, O. V. Przhonska, S. Yao, *J. Photochem. Photobiol. A: Chem.* **2006**, *184*, 105.
[29] a) Y. Ren, J. W. Y. Lam, Y. Dong, B. Z. Tang, K. S. Wong, *J. Phys. Chem. B* **2005**, *109*, 1135; b) Y. Ren, Y. Dong, J. W.Y. Lam, B. Z. Tang, K. S. Wong, *Chem. Phys. Lett.* **2005**, *402*, 468.
[30] Y. Gao, Y. Qu, T. Jiang, H. Zhang, N. He, B. Li, J. Wu, J. Hua, *J. Mater. Chem. C* **2014**, *2*, 6353.
[31] a) B. Li, R. Tong, R. Zhu, F. Meng, H. Tian, S. Qian, *J. Phys. Chem. B* **2005**, *109*, 10705; b) Y. H. Jiang, Y. C. Wang, J. L. Hua, S. Y. Qu, S. Q. Qian, H. Tian, *J. Polym. Sci., Part A: Polym. Chem.* **2009**, *47*, 4400.
[32] a) F. S. Meng, J. Mi, S. X. Qian, K. C. Chen, H. Tian, *Polymer* **2003**, *44*, 6851; b) J. L. Hua, B. Li, F. S. Meng, F. Ding, S. X. Qian, H. Tian, *Polymer* **2004**, *45*, 7143.